Inorganic Chemistry

Article

pubs.acs.org/IC

Study of Ga^{3+}-Induced Hydrothermal Crystallization of an α-Quartz Type $Ga_{1-x}Fe_xPO_4$ Single Crystal by *in Situ* X-ray Absorption Spectroscopy (XAS)

Manhal Souleiman,[†,‡] Olivier Cambon,*[,†] Abel Haidoux,[†] Julien Haines,[†] Claire Levelut,[‡] Vincent Ranieri,[§] and Jean-Louis Hazemann[∥]

[†]Institut Charles Gerhardt Montpellier, Equipe C2M, UMR CNRS-UM2-ENSCM-UM1 5253, Université Montpellier 2, Place Eugène Bataillon, CC1504, 34095 Montpellier Cedex 5, France

[‡]Laboratoire Charles Coulomb, Département Colloïdes, Verres et Nanomatériaux, UMR CNRS-UM2 5221, Université Montpellier 2, Place Eugène Bataillon, CC026, 34095 Montpellier Cedex 5, France

[§]CEA-INAC, 17 Rue des Martyrs, 38054 Grenoble Cedex 9, France

[∥]Institut Néel, Département MCMF, CNRS-Grenoble, 25 Avenue des Martyrs, B.P.166, 38042 Grenoble Cedex 9, France

ABSTRACT: The dissolution of α-$FePO_4$ and the α-$Ga_{0.75}Fe_{0.25}PO_4$ solid solution with α-quartz-type structures under hydrothermal conditions in 1 M HNO_3 aqueous solution was investigated by *in situ* X-ray absorption spectroscopy (XAS) at the Fe K-edge. The solubility of α-$FePO_4$ increases with temperature and is higher at 25 MPa than at 50 MPa. The Fe^{3+} cation in solution is 6-fold coordinated with an average Fe−O distance close to 2.0 Å. A similar experiment was performed with a solid solution of α-quartz-type $Ga_{0.75}Fe_{0.25}PO_4$ as the starting phase under a pressure of 25 MPa. By varying the temperature from 303 K up to 573 K a single crystal was grown with 23% Fe^{3+} with the α-quartz-type structure. These results show that the crystallization of pure α-quartz-type $FePO_4$ by the hydrothermal method is not possible due to the formation of very stable Fe^{3+} hexa-aquo complexes $[Fe(H_2O)_6]^{3+}$ and to the absence of FeO_4 tetrahedra in solution. Ga^{3+} cations in solution induce the formation of gallophosphate complexes at the solid−liquid interface, which are at the origin of the nuclei for crystallization. We propose a crystallization mechanism in which the Fe^{3+} substitutes Ga^{3+} with a 4-fold coordination in mixed (iron/gallo)-phosphate complexes that leads to the growth of an α-quartz-type $Ga_{0.77}Fe_{0.23}PO_4$ single crystal.

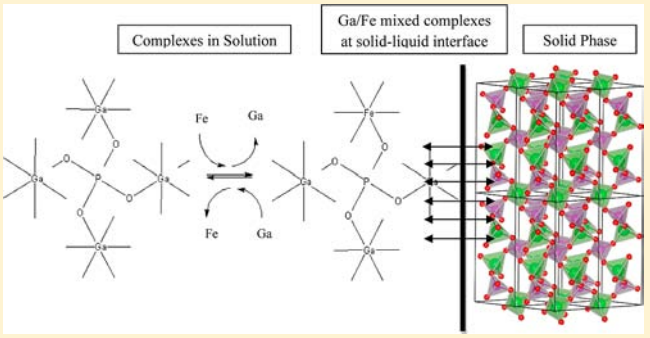

1. INTRODUCTION

Physical properties (dielectric, piezoelectric, etc.) of piezoelectric materials are often limited by the thermal stability. New applications require materials with high piezoelectric performance and with good thermal stability. α-Quartz homeotypes belonging to $P3_121$ or $P3_221$ space group and with the $M^{III}X^{V}O_4$ (M = Al, Ga, Fe; X = As, P)[1−18] general formula are promising candidates. The piezoelectric properties and thermal stability are linked to the structural distortion of the α-phase with respect to the β-phase. The structural distortion can be described by two angles:[11] the intertetrahedral bridging angle θ and the tetrahedral tilt angle δ ($\delta = 0°$ for β-quartz). $GaAsO_4$ and GeO_2, which are the most distorted materials with the lowest θ and the highest δ values, exhibit the highest piezoelectric coupling coefficients and the highest thermal stability.[12] Among the quartz isotypes, $GaPO_4$ has been widely studied, its structural ($\delta = 23.3°$, $\theta = 134.4°$)[18] and piezoelectric properties are well-defined (coupling electromechanical coefficient k = 16%).[15]

$FePO_4$ is also a potentially interesting piezoelectric material. The crystal structure of $FePO_4$ has been studied ($\delta = 21.5°$, $\theta = 137.8°$) under ambient conditions and as a function of temperature.[14,19] The structural distortion of $FePO_4$ is similar to that of $GaPO_4$, and a similar piezoelectric coupling coefficient can be expected at room temperature. The hydrothermal synthesis of $FePO_4$ gives rise to several hydrated phases such as strengite, phosphosiderite (metastrengite) ($FePO_4{\cdot}nH_2O$), and ferric giniite $Fe_5(PO_4)_4(OH)_3{\cdot}2H_2O$ depending on the hydrothermal conditions.[20,21] The structures of these compounds are built up of PO_4 tetrahedra and FeO_6 octahedra. At high temperature, strengite and phosphosiderite transform to α-quartz-type $FePO_4$.[19,22] Until now, no single crystal of α-quartz $FePO_4$ has been grown by using the hydrothermal method. Because of the difficulty to grow a pure $FePO_4$ single crystal, α-quartz $Ga_{1-x}Fe_xPO_4$ has been studied.[23] The same approach has been already adopted for different α-

Received: August 8, 2012
Published: October 11, 2012

quartz-type solid solutions, several of which have been prepared: SiO_2-GeO_2,[24−27] SiO_2-PON,[28] SiO_2-AlPO_4,[29] $AlPO_4-GaPO_4$,[30−33] $AlPO_4-AlAsO_4$,[30] $AlPO_4-FePO_4$,[29] $GaPO_4-FePO_4$.[30] In the particular case of the SiO_2-GeO_2 binary solid solution, in order to optimize the conditions for crystal growth, the dissolution of $Si_{1-x}Ge_xO_2$ ($0.2 < x < 0.5$) solid solutions under hydrothermal conditions was studied by *in situ* X-ray absorption spectroscopy at the Ge K-edge.[27] The analysis of the absorption spectra provided information about the dissolution kinetics and the local structure around Ge atoms as a function of the solvent and solid solution composition. The structure and reaction mechanisms of Fe^{3+} in aqueous solution have been studied by X-ray absorption (spectra recorded at K-edge) and Raman spectroscopy,[36,37] showing the Fe^{3+} hydration with an octahedral coordination forming $[Fe(H_2O)_6]^{3+}$ complexes. In addition, the study of Ga^{3+} in aqueous solution by XAS also confirms the 6-fold coordination around Ga^{3+} by six water molecules with a Ga−O distance of 1.956 Å.[38]

A similar approach was adopted in the present study, which focuses on the effect of hydrothermal conditions on the local structural environment of the Fe atom during the dissolution of α-$FePO_4$ and α-$Ga_{0.75}Fe_{0.25}PO_4$ and the mechanisms of nucleation and crystallization in 1 M HNO_3 by *in situ* X-ray absorption spectroscopy (XAS).

2. EXPERIMENTAL SECTION

2.1. Sample Preparation. α-Quartz-type $FePO_4$ was obtained by heating pellets of $FePO_4{\cdot}2H_2O$ (Strengite, Sigma-Aldrich) at 873 K for 24 h and checked by X-ray diffraction (XRD). A $Ga_{1-x}Fe_xPO_4$ (x = 0.25) solid solution was prepared from a mixture of $GaPO_4$ ($GaPO_4$ powder was synthesized by a hydrothermal method[4,5]) and $FePO_4{\cdot}2H_2O$. A pellet was compressed at 2 tons for 5 min. This mixture was heated at 1148 K for 7 days in air, and the final products were characterized by XRD. The solvent used for hydrothermal experiments was 1 M HNO_3.

2.2. X-ray Absorption Experiments under Hydrothermal Conditions. XAS spectra were recorded at Fe K-edge (7.112 keV)[35] in transmission/fluorescence modes simultaneously with a beam size of 300 × 200 μm^2 at the BM30B FAME (French absorption beamline in materials and environmental sciences) beamline of the European Synchrotron Radiation Facility (ESRF) in Grenoble.[39,40] The X-ray beam produced by the source was focused in the horizontal plane by a Si (220) double-crystal as a monochromator and by two Rh-coated mirrors in the vertical plane. The beam position is fixed during the acquisition for all experiments. A high temperature autoclave with three Be windows was used for high pressure experiments. This autoclave can be used in transmission and fluorescence modes.[41] The solid sample and the solution were placed in a HP/HT cell made of glassy carbon (internal diameter = 4.0 mm, length = 85 mm). The cell is completely full. Inside the tube, two carbon pistons transmit the pressure generated by high-purity helium gas. The pressure is controlled by high-pressure strain gauges. A molybdenum resistive heater was used to heat the cell, and temperature was controlled by using two calibrated K-type (Pt−Pt/Rh) thermocouples. The autoclave was cooled by a water jacket. During the experiments, pressure was applied before heating the cell. The temperature in the cell was calibrated by calculating the density of distilled water as a function of pressure and temperature based on XAS measurements and comparing it with values from the National Institute of Standard and Technology.[42]

2.3. XAS Spectra. *2.3.1. Extended X-ray Absorption Fine Structure, EXAFS.* The EXAFS oscillations are related to the local structure around the iron atom in solution[43] and the absorption jump ($\Delta\mu$) to the concentration, respectively. In transmission mode, $\Delta\mu$ can be obtained as follows

$$\Delta\mu = \Delta\sigma_{Fe} x M_{Fe} m_{Fe} d_{fluid}$$

where $\Delta\sigma_{Fe}$ is the variation of the total absorption cross section of Fe at the K-edge (cm^2/g), x is the optical path length inside the cell (cm), M_{Fe} is the atomic mass, m_{Fe} is the molal aqueous Fe concentration (mol/kg of solution), and d_{fluid} is the density of the aqueous solution (g/cm^3) at a given T and P.[44]

Even if this formula is not applicable in fluorescence mode, the evolution of the height of the absorption edge corresponds to the variation of the concentration of the absorbing element in solution at a given T and P. The absorption edge height ($\Delta\mu$) was calculated from the difference between the fitted curves (spline curves) for the pre-edge and postedge of the absorption signal. EXAFS signals were analyzed using the Athena software for signal extraction (IFEFFIT) and by Artemis for fitting the EXAFS spectra.[45] The signal was normalized, and then the EXAFS oscillations $\chi(k)$ were extracted. The distance to the neighboring shells and EXAFS Debye−Waller factor were fitted. The error in determining the edge energy ΔE_0 was also fitted. The amplitude factor (So^2) was fixed to 0.7. All fits were performed in R space.

2.4. EPMA and Raman Spectroscopy. The chemical composition of the single crystal ($Ga_{1-x}Fe_xPO_4$) was studied using an electron probe microanalyzer (EPMA CAMECA SX 100) with five wavelength dispersive X-ray spectrometers (WDS). Single crystals were embedded in epoxy resin and then polished. A focused beam of 10 nA under 20 kV of accelerating voltage with counting times of ∼30 s was used for analyses using Fe, P, and Ga Kα lines. Calibration was performed using Ga_2O_3, $AlPO_4$, and Fe_2O_3 as standard materials. Raman measurements were performed on a Horiba Jobin-Yvon Labram Aramis Raman spectrometer using a blue diode laser (λ = 473 nm).

2.5. Single Crystal XRD. The structure of the $Ga_{0.77}Fe_{0.23}PO_4$ single crystal was determined by using XRD-data obtained with an Agilent Xcalibur 4-circle diffractometer equipped with a CCD detector using Mo Kα radiation (λ = 0.7107 Å). The intensity data were collected using the Crysalis CCD program. The cell parameters were refined, and the intensity data were reduced and corrected for absorption using the Crysalis RED program. The structure of the single crystal was refined by using SHELXL-97 software.[46]

3. RESULTS AND DISCUSSION

3.1. Solid References. The XAS spectra were recorded in transmission mode at the Fe K-edge (Figure 1) for solid samples of α-$FePO_4$ and α-$Ga_{0.75}Fe_{0.25}PO_4$. These spectra allow the tetrahedral environment around the iron atom, the energy position at Fe K-edge, and the pre-edge peak intensity

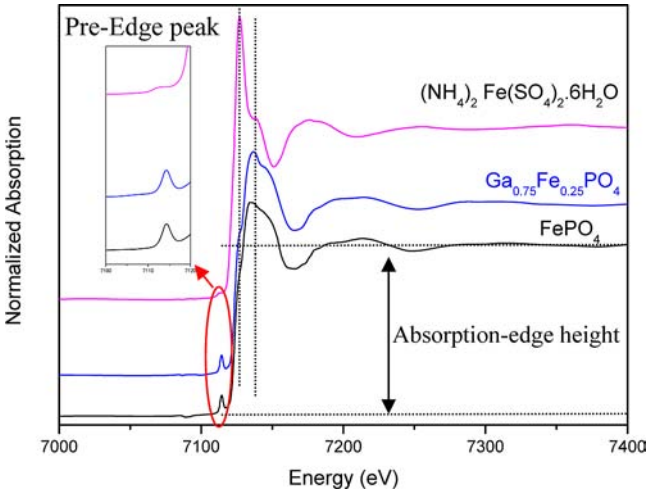

Figure 1. Transmission XAS spectra of Fe during the dissolution of α-$FePO_4$ and α-$Ga_{0.75}Fe_{0.25}PO_4$ (Fe^{3+} K-edge at 7.136 KeV) and $(NH_4)_2Fe(SO_4)_2{\cdot}6H_2O$ (Fe^{2+} K-edge at 7.127 keV) at room temperature.

dx.doi.org/10.1021/ic3017485 | Inorg. Chem. 2012, 51, 11811−11819

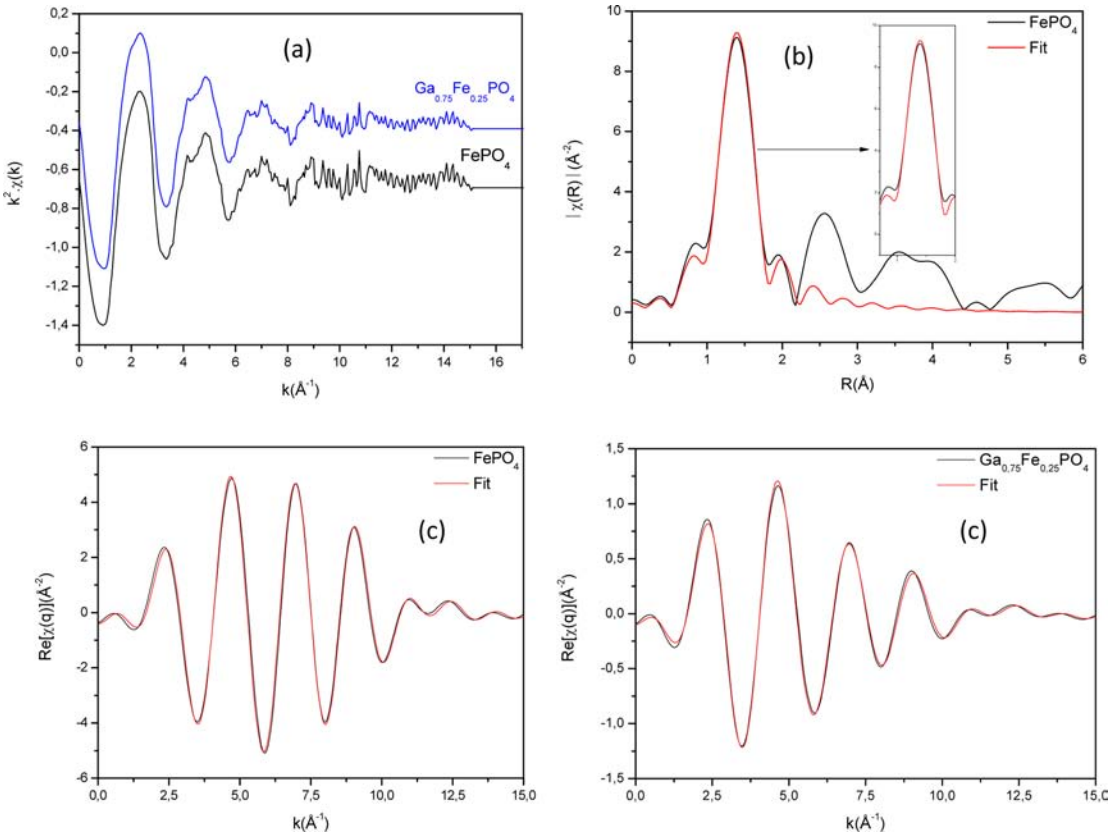

Figure 2. (a) Normalized ($k^2 \cdot \chi(k)$) Fourier transform for the first neighbor atoms measured in transmission mode at the Fe K-edge. (b) Example of a Fourier transform for $FePO_4$ in R space with the window used to isolate the peak related to the first shell of atoms. (c) Inverse Fourier transform fitted by using a FeO_4 tetrahedral model.

associated with the 4-fold coordination to be characterized. A $(NH_4)_2Fe(SO_4)_2 \cdot 6H_2O$ sample with Fe^{2+} with an octahedral local structure around the iron atom was also studied. The XAS spectrum related to the octahedral environment of Fe^{2+} is characterized by a very weak pre-edge peak and a shift of the main edge jump to a lower energy in comparison with the main edge jump of Fe^{3+} with a tetrahedral environment. The two oxidation states of iron can be distinguished (E = 7.127 keV for Fe^{2+}, E = 7.135 keV for Fe^{3+}). The presence of a pre-edge peak is due to the 1s→ 3d electronic transition, which is located at about 20 eV before the Fe K-edge.[47,48] The intensity of the pre-edge peak is greater for tetrahedral FeO_4 in $FePO_4$ and $Ga_{0.75}Fe_{0.25}PO_4$ than for octahedral FeO_6 in $(NH_4)_2Fe(SO_4)_2 \cdot 6H_2O$. The analysis was limited to the first layer of atoms around the iron atom with a tetrahedral model by using a Hann-type window to select the range for the first shell neighbors of the iron atom (Figure 2b). The results of fits are shown in Table 1. The Fe−O distance of 1.85 Å is in good agreement with the interatomic distance of iron in 4-fold coordination.[14]

Table 1. Fe K-Edge EXAFS Data for $FePO_4$ in the Solid State[a]

samples	k (Å)$^{-1}$	Fe−O (Å)	σ^2 (Å^2) × 10^{-3}
$FePO_4$	2−10	1.85 (1)	2.0(5)
$Ga_{0.75}Fe_{0.25}PO_4$	2−10	1.84(1)	2.7(1)

[a]Factor-R ∼ 0.0001−0.0008, ΔE (eV) = −1.95(1) to −1.10(2), χ_{red} ∼ 1.98−5.60, S_0^2 = 0.70, and N_0 = 4.0.

3.2. Dissolution of α-Quartz $FePO_4$. The dissolution of α-$FePO_4$ solid samples was studied in nitric acid solutions under different hydrothermal conditions (Figure 3). The absorption edge height during the dissolution of $FePO_4$ (10.8 mg) under 25 MPa in 1 M HNO_3 (0.21 mL) presents a maximum value at 518 K (Figure 3a,b) and then drastically decreases after 20 h due to a crystallization process. In the case of the dissolution of $FePO_4$ (11.2 mg) in 1 M HNO_3 (0.18 mL) under 50 MPa up to 618 K (Figure 3c,d), the absorption edge height increases up to 393 K and remains quite stable at higher temperature. At 25 and 50 MPa, these results demonstrate that the iron concentration increases as a function of temperature with only small variations. At 25 MPa, the decrease in iron concentration at 518 K is due to the crystallization of $FePO_4 \cdot 2H_2O$ as confirmed by Raman spectroscopy. This result demonstrates that $FePO_4 \cdot 2H_2O$ is thermodynamically more stable than the α-quartz phase under hydrothermal conditions. In aqueous solution, iron crystallizes preferentially in 6-fold coordination. The α-quartz phase was completely dissolved and recrystallizes to give $FePO_4 \cdot 2H_2O$ at the end of the experiment. At 50 MPa, the iron concentration does not decrease, because the time of observation is shorter than for 25 MPa and no crystallization was observed; only a small quantity of the initial sample was recovered. This proves that HNO_3 at 50 MPa is a less efficient solvent than at 25 MPa. Moreover, the absorption edge height in dilute nitric acid is higher at 25 MPa than at 50 MPa (Figure 3). This result can be explained by the behavior of nitric acid under pressure.[49] The increased pressure enhances the formation of an H-bonded polymer-like compound that

dx.doi.org/10.1021/ic3017485 | Inorg. Chem. 2012, 51, 11811−11819

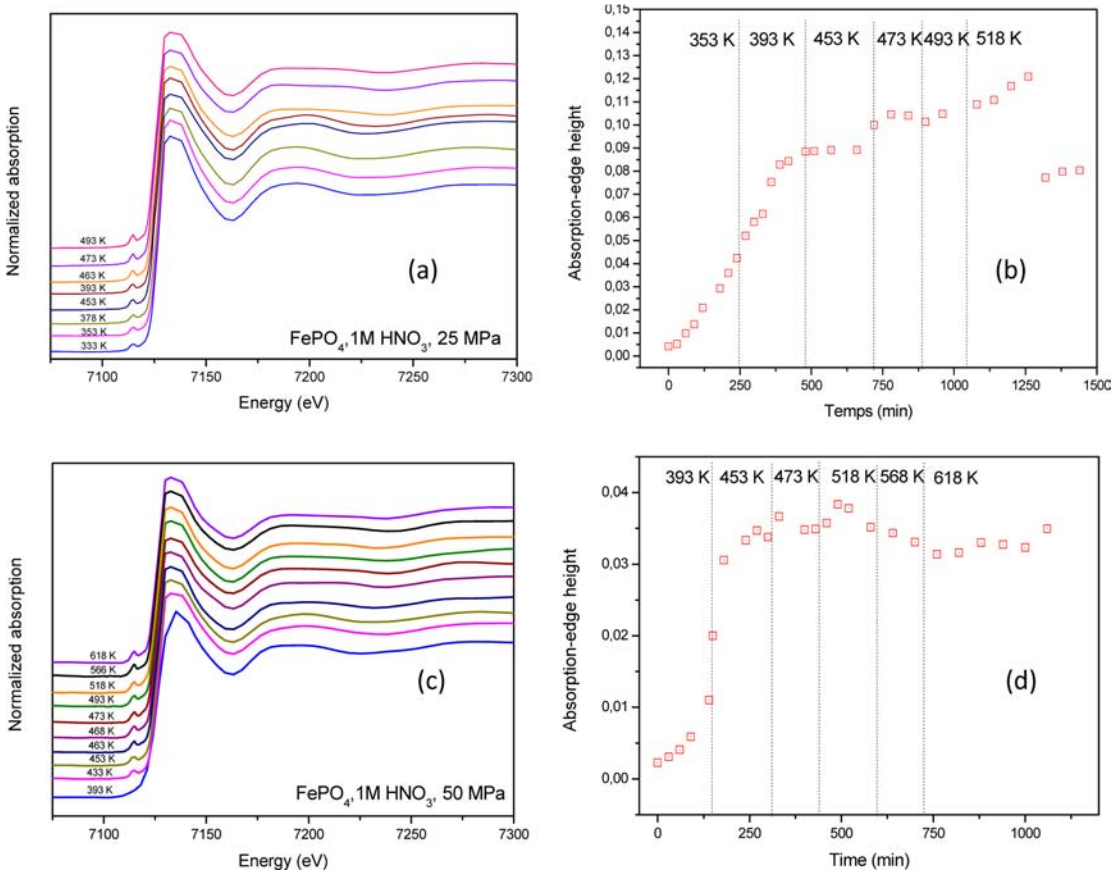

Figure 3. Normalized XAS spectra for the *in situ* dissolution of $FePO_4$ at the Fe K-edge in 1 M nitric acid at (a) 25 MPa and (c) 50 MPa and different temperatures. Absorption-edge height as a function of time and temperature at (b) 25 MPa, (d) 50 MPa.

decreases the strength of the nitric acid limiting the dissolution capability of the solvent.

3.3. Analysis the Local Structure around the Iron Atom in 1 M HNO_3 from XAS Spectra. *a. Pre-Edge Peak Features.* According to Wilke et al.,[47] pre-edge peaks in XANES spectra for FeO_6 octahedra are less intense compared to that for FeO_4 tetrahedra. The intensities of the pre-edge peak is related to the coordination around the iron atom. The intensity of the pre-edge peaks (Figure 4) in XANES spectra of $FePO_4$ in 1 M HNO_3 solution are lower compared to that in the solid state, which confirms the formation of octahedral environment around the iron atom in solution. Pokrovski et al[50] have shown that the Fe^{3+} ions undergo rapid hydration in acidic solutions and form octahedral coordinated species. On the basis of the analysis of XANES pre-edge, the solvated iron in dilute nitric acid forms FeO_6 octahedra with six oxygen atoms under pressure and temperature.

b. EXAFS Analysis. XAS spectra of Fe^{3+} in 1 M HNO_3 present clear EXAFS oscillations that can be analyzed to study the local structure around the iron atom in solution. The same procedure used as previously for the solid state was applied for analyzing the local structure except that an octahedral environment was considered. The $K^2{\cdot}\chi(k)$ oscillations (Figure 5a) are very similar. The $\mathrm{Re}[\chi(q)]$ component is fitted in k space for 6.0 neighboring oxygen atoms in the first shell, leading to a good fit to the experimental signal (Figure 5c). An interatomic Fe−O distance in solution of about ∼2.0 Å was obtained (Table 2), which is in good agreement with the literature[36,37,51] for an octahedral Fe^{3+} environment with six oxygen atoms forming $[Fe(H_2O)_6]^{3+}$ complex species. The

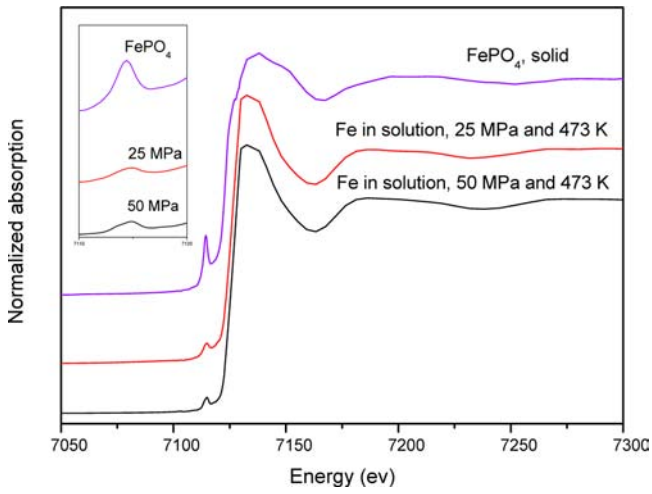

Figure 4. XANES spectra at the Fe K-edge and pre-edge peak of the XANES spectra at the Fe K-edge of $FePO_4$ in the solid state and in solutions under different hydrothermal conditions.

Fe−O distance is not affected by temperature and pressure. The Debye−Waller factor (σ^2) is higher in solution (Table 2) compared to the solid state (Table 1). This can be explained by the dynamics of the exchange of water molecules around the iron atom in solution. The EXAFS analysis confirms the octahedral environment around Fe^{3+} in solution at high pressure and temperature.

3.4. Dissolution and Crystallization of α-Quartz $Ga_{1-x}Fe_xPO_4$ by *in Situ* XAS. *a. In Situ XAS.* The dissolution

dx.doi.org/10.1021/ic3017485 | Inorg. Chem. 2012, 51, 11811−11819

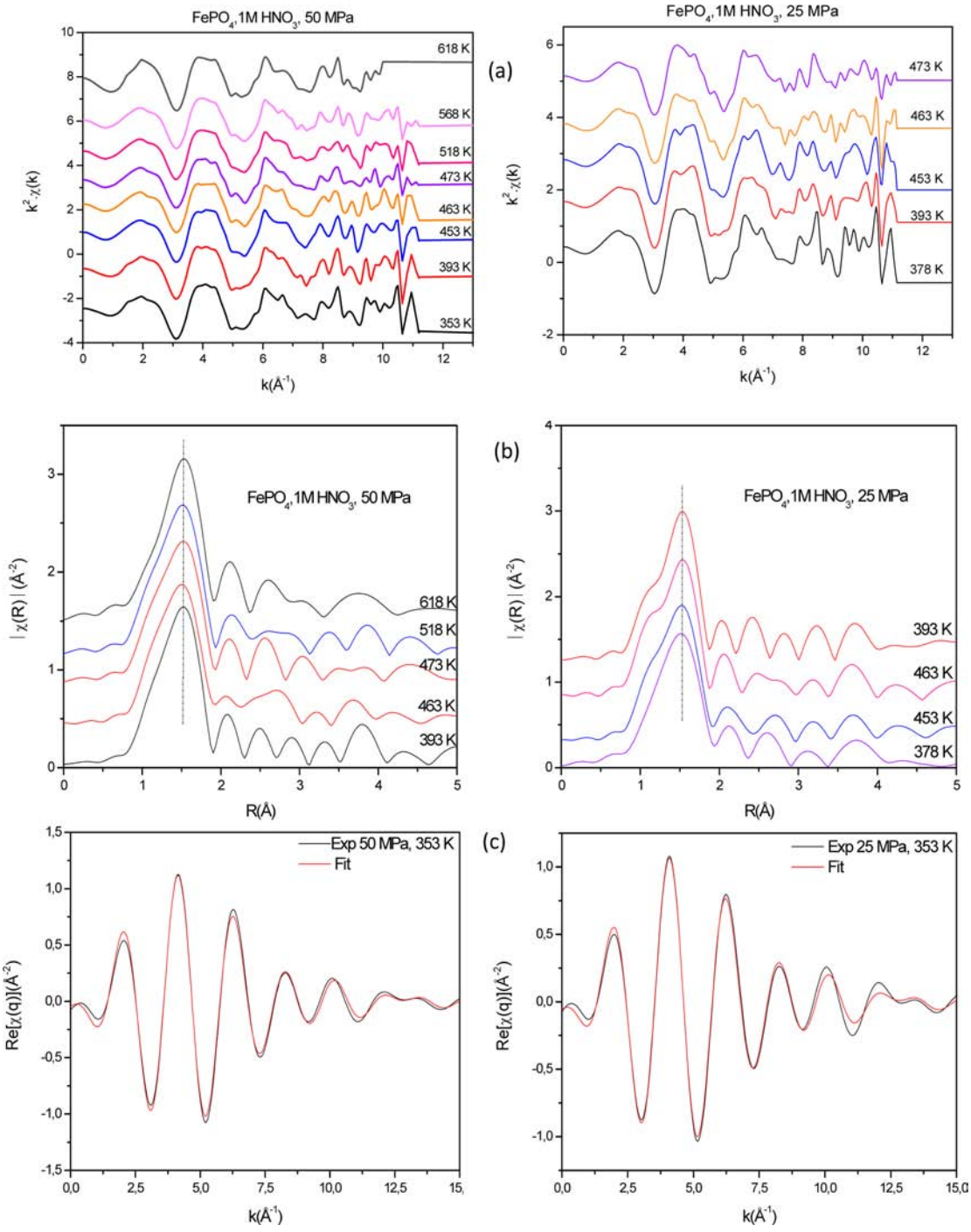

Figure 5. Normalized ($k^2 \cdot \chi(k)$) at 25 MPa, 50 MPa and different temperatures: (a) Fourier transform for the first neighbor atoms measured in fluorescence mode at Fe K-edge, (b) Fourier transform in R space, (c) inverse Fourier Transform fitted by using a FeO_6 octahedral model.

of the α-$Ga_{0.75}Fe_{0.25}PO_4$ solid solution (7.1 mg) in 1 M HNO_3 (0.23 mL) at 25 MPa from 303 to 568 K for 12 h was studied (Figure 6a) by *in situ* XAS. The drastic decrease of the absorption-edge height at 518 K after 10 h of dissolution is due to crystallization (Figure 6b). At the end of the experiment, no unreacted powder was present in the bottom of the cell; only one single crystal was obtained. The quality of the EXAFS oscillations was not sufficient to extract further information about the local structure around the iron atom during the dissolution.

b. Crystal Structure of $Ga_{0.77}Fe_{0.23}PO_4$. After the dissolution experiment, a 172 × 75 × 60 μm^3 single crystal was obtained and characterized by EPMA and single crystal XRD. The composition is 23% at. Fe ($Ga_{0.77}Fe_{0.23}PO_4$). The structure was refined by SHELXL-97 (Tables 3−8). The structural parameters and agreement factors of the structural refinement indicate that the crystal is of an excellent crystalline quality. The fractional atomic coordinates, bond distances M−O, and angles θ and δ are found to vary continuously as a function of the composition which was fixed to the EPMA values. According to the refinement results, the cell parameters a and c, the cell

dx.doi.org/10.1021/ic3017485 | *Inorg. Chem.* 2012, 51, 11811−11819

Table 2. EXAFS Fitting Parameters[a]

T (K)	k (Å)$^{-1}$	Fe−O (Å)	σ^2 (Å^2) × 10^{-3}
	P = 25 MPa, Fe−O(Å)[36,37] = 1.99, 2.10		
303	2−15	1.99(1)	6.8(2)
323	2−15	1.99(1)	5.7(2)
333	2−15	1.99(1)	4.7(1)
353	2−15	1.99(1)	4.8(2)
378	2−15	1.99(1)	5.2(1)
393	2−15	2.00(1)	6.0(2)
453	2−15	2.01(1)	5.8(2)
463	2−15	1.99(1)	7.0(3)
473	2−15	1.99(3)	4.3(5)
	P = 50 MPa, Fe−O(Å)[36,37] = 1.99, 2.10		
303	2−15	1.99(1)	6.8(2)
323	2−15	1.99(1)	5.7(2)
333	2−15	1.99(1)	4.7(1)
353	2−15	1.99(1)	4.8(2)
378	2−15	1.99(1)	5.2(1)
393	2−15	2.00(1)	6.0(2)
453	2−15	2.01(1)	5.8(2)
463	2−15	1.99(1)	7.0(3)

[a] R-factor ∼ 0.002−0.016, ΔE (eV) = −5.78(5) to −1.22(1), χ_{red} ∼ 1.3-9.90, S_0^2 = 0.7, and N_0 = 6.0.

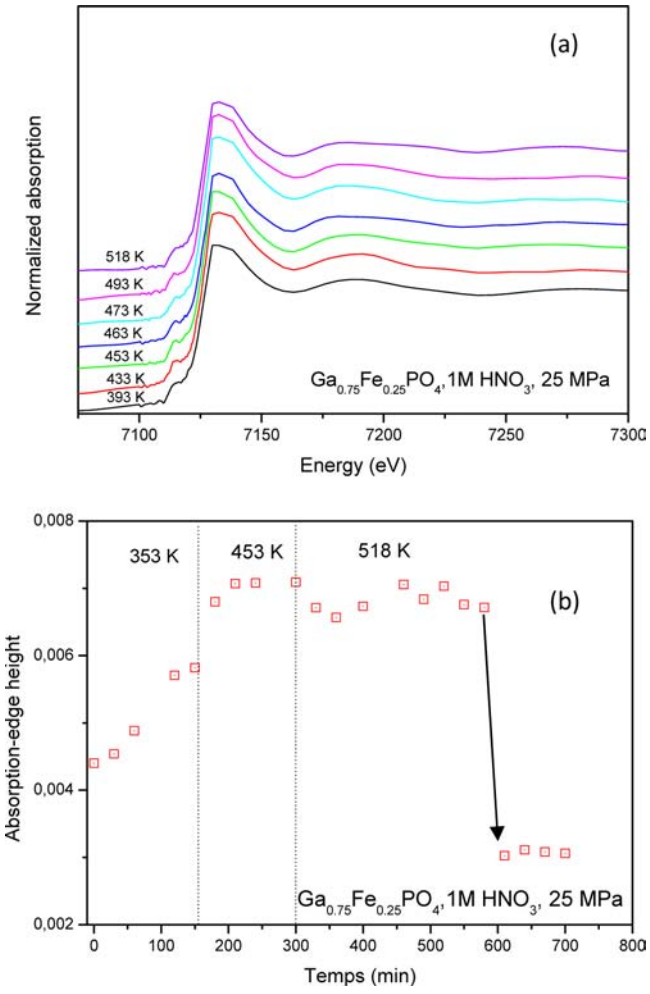

Figure 6. (a) XAS spectra and (b) absorption-edge height during the dissolution of $Ga_{0.75}Fe_{0.25}PO_4$ at 25 MPa.

Table 3. Experimental Data: Single Crystal X-ray Diffraction

	$Ga_{0.77}Fe_{0.23}PO_4$
T (K)	293(2)
cryst syst	trigonal
space group	$P3_221$
$a = b$ (Å)	4.92938(3)
c (Å)	11.0940(6)
V (Å^3)	233.45(1)
h, k, l	$-7 \le h \le 7$
	$-7 \le k \le 7$
	$-16 \le l \le 16$
density (g/cm^3)	3.43
diffractometer	Agilent Xcalibur
radiation type	Mo Kα
wavelength	0.7107
abs corr	numerical
μ (mm^{-1})	8.236
$R_{equivalents}$	0.023
R_σ	0.009
no. measured reflections	8926
no. unique reflns	555
no. obsd reflns ($I > 2\sigma$)	543
	Refinement
R	0.0227
R_W	0.071
χ^2	1.44
no. params	29
extinction coeff	0.015(2)
weighting scheme	$w = (\sigma^2 F_o^2 + 1.24P)^{-1}$ where $P = (F_o^2 + 2F_C)/3$

Table 4. Fractional Atomic Coordinates and Equivalent Isotropic Displacement Parameters (Å^2) for $Ga_{0.77}Fe_{0.23}PO_4$

	x	y	z	100 × U_{eq}
Ga/Fe	0.4567(1)	0	−0.333	0. 76 (3)
P	0.4562(3)	0	−0.833	0.81(2)
O1	0.408(1)	0.2698(7)	−0.8728(3)	1.47(6)
O2	0.5907(9)	−0.0918(8)	−0.9399(3)	1.47(6)

volume, and the M−O distances increase linearly as a function of composition x (Figure 7) between the two end-members $GaPO_4$ and $FePO_4$. The degree of distortion decreases with x (θ increases and δ decreases). The structure is shown in Figure 8.

In the $Al_{1-x}Ga_xPO_4$ solid solution, the structural distortion (i.e., θ and δ) is found to vary continuously as a function of composition between the pure end members, $AlPO_4$ and $GaPO_4$ (θ decreases and δ increases with x[33]). In the case of $Al_{1-x}Ga_xPO_4$ the structural evolution is opposite to that of $Ga_{1-x}Fe_xPO_4$: the cell volume is constant due to the almost identical nonbonded radii of Al^{3+} and Ga^{3+} (1.62 and 1.63 Å, respectively). In this case, the greater value of the ionic radius for Ga^{3+} (0.47 Å) compared to this of Al^{3+} (0.39 Å) leads to an increase of the degree of the distortion by increasing x. For $Ga_{1-x}Fe_xPO_4$, the observed behavior can be explained by the nonbonded radii of Ga^{3+} and Fe^{3+} cations. Indeed, the nonbonded radius of Fe^{3+} (1.68 Å) is greater than that of Ga^{3+} (1.63 Å)[32] leading to an increase of the M−P distance (Ga−P = 3.085 Å and Fe−P = 3.16 Å)[52,54] and in consequence to an increase in unit cell volume. In spite of the larger ionic radius of Fe^{3+} (0.49 Å) compared to Ga^{3+} (0.47 Å),[55] the increase of the cell volume makes that the structure becomes

dx.doi.org/10.1021/ic3017485 | Inorg. Chem. 2012, 51, 11811−11819

Table 5. Anisotropic Atomic Displacement Parameters (Å^2) for α-Quartz-Type $Ga_{0.77}Fe_{0.23}PO_4$

	$100 \times U_{11}$	$100 \times U_{22}$	$100 \times U_{33}$	$100 \times U_{23}$	$100 \times U_{13}$	$100 \times U_{12}$
Ga/Fe	0.87(2)	0.69(3)	0.67(2)	0.06(3)	0.032(1)	0.34(2)
P	0.90(4)	0.75(6)	0.73(5)	0.07(6)	0.03(3)	0.38(3)
O1	2.1(2)	1.3(1)	1.4(1)	0.54(1)	0.57(2)	1.18(2)
O2	2.1(2)	1.1(2)	1.3(1)	−0.08(1)	0.45(1)	0.89(1)

Table 6. Selected Bond Distances (Å) in α-Quartz-Type $Ga_{0.77}Fe_{0.23}PO_4$

	M−O1	M−O2	P−O1	P−O2
$GaPO_4$[18]	1.814	1.820	1.528	1.527
$Ga_{0.77}Fe_{0.23}PO_4$	1.832(3)	1.821(3)	1.527(4)	1.530(3)
$FePO_4$[14]	1.858	1.858	1.531	1.521

Table 8. Intertetrahedral Bridging and Tilt Angles (deg) in α-Quartz-Rype $Ga_{0.77}Fe_{0.23}PO_4$

	θ(M−O−X)	δ
$GaPO_4$[18]	134.6	23.4
$Ga_{0.77}Fe_{0.23}PO_4$	135.2(1)	22.98(8)
$FePO_4$[14]	137.8	21.5

less distorted when Fe^{3+} cation substitutes Ga^{3+} in the α-quartz solid solution. The changes in the angles (θ and δ) correspond to a decrease of degree of distortion with an increase of the Fe^{3+}-content: θ increases and δ decreases with x (Table 8).

c. Role of Ga^{3+} in the Crystallization Process. The analysis of EXAFS oscillations during the dissolution of α-$Ga_{0.75}Fe_{0.25}PO_4$ in 1 M HNO_3 confirms the immediate formation of 6-fold coordination around the iron atom. Previously, pure $GaPO_4$ crystal growth has been studied by ^{31}P and ^{71}Ga NMR spectroscopy.[53] The presence of hexa-aqua-gallium complexes $[Ga(H_2O)_6]^{3+}$ has been confirmed, but in presence of phosphate groups gallophosphate species have been observed and considered to be the most reactive units for the crystal growth process.

The existence of species containing Ga^{3+} and P^{5+} in acidic solutions governs the crystallization of an α-quartz structure with GaO_4 and FeO_4 tetrahedra. Even if the Fe^{3+} ions are 6-fold coordinated in solution, the presence of gallophosphate species induces the crystallization in α-quartz structure. On the basis of the mechanism of $GaPO_4$ growth, we propose that the crystallization mechanism of mixed α-quartz $Ga_{1-x}Fe_xPO_4$ requires the formation of a mixed Ga/Fe phosphate complex at the solid−liquid interface, which is at the origin of the crystallization of the α-quartz-type solid solution with 4-fold coordinated iron.

4. CONCLUSION

The dissolution of $FePO_4$ and α-$Ga_{0.75}Fe_{0.25}PO_4$ solid solution under hydrothermal conditions in 1 M HNO_3 was studied by *in situ* XAS at the Fe K-edge. The height of the absorption edge indicates the low solubility of $FePO_4$, and the analysis of the EXAFS oscillations provides information about the local structure around the Fe^{3+} atom under hydrothermal conditions. Fe^{3+} in 1 M HNO_3 is 6-fold coordinated to oxygen (with a Fe−O distance of about 2.0 Å), which prevents the crystallization of an α-quartz-type structure in dilute acid. In the case of the dissolution of α-$Ga_{0.75}Fe_{0.25}PO_4$ in 1 M HNO_3 at 25 MPa and 303 K $\leq T \leq$ 573 K, crystallization of an α-quartz-type solid solution occurs. The structure of a single crystal grown by this method was refined using X-ray diffraction data. A piezoelectric material based on the $GaPO_4$−$FePO_4$ solid solution with the α-quartz structure was thus synthesized by hydrothermal

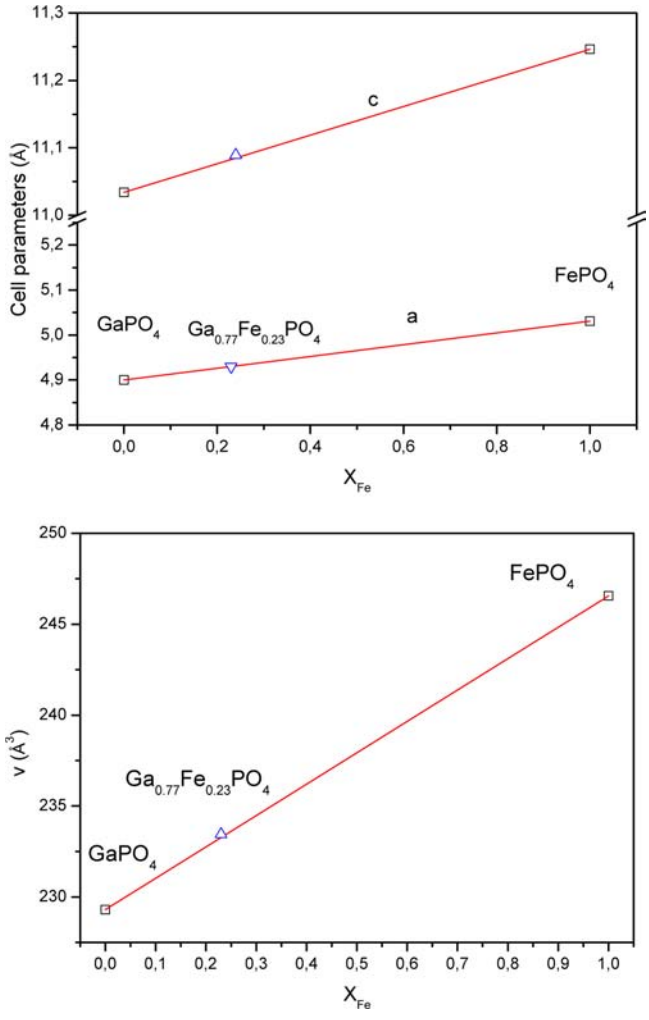

Figure 7. Plot of a and c cell parameters and the unit cell volume V as a function of composition x in $Ga_{1-x}Fe_xPO_4$.

Table 7. Tetrahedral Bond Angles (deg) in α -Quartz-Type $Ga_{0.77}Fe_{0.23}PO_4$

	O2−M−O2	O1−M−O1	O1−M−O2	O1−M−O2	O1−P−O1	O1−P−O2	O1−P−O2	O2−P−O2
$GaPO_4$[18]	111.8	111.8	110.3	105.4	109.6	108.0	111.8	107.7
$Ga_{0.77}Fe_{0.23}PO_4$	112.1(2)	113.3(2)	110.4(2)	105.4(2)	107.6(3)	108.4(2)	111.8(2)	109.0(3)
$FePO_4$[14]	111.6	114.3	109.3	106.3	108.5	107.7	112.0	109.0

dx.doi.org/10.1021/ic3017485 | Inorg. Chem. 2012, 51, 11811−11819

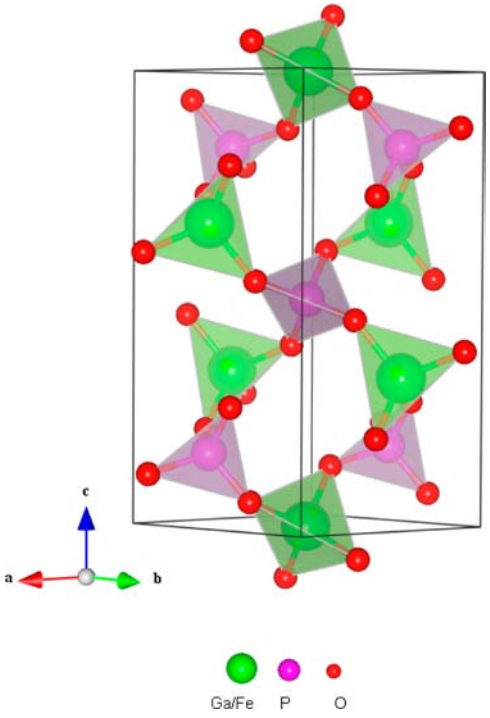

Figure 8. Crystal structure of $Ga_{0.77}Fe_{0.23}PO_4$.

methods. A crystallization mechanism is proposed with the formation of mixed Ga/Fe phosphate complexes, which enable the growth of an α-quartz-type crystal with FeO_4 tetrahedra by using hydrothermal methods. This route could be extended to grow in acidic solutions new $[FeO_4]$-based materials like new multiferroelectrics.

AUTHOR INFORMATION

Corresponding Author

*E-mail: olivier.cambon@univ-montp2.fr.

Notes

The authors declare no competing financial interest.

ACKNOWLEDGMENTS

The authors thank the CRG and FAME team, C. Merlet (Service Microsonde Sud, Université Montpellier 2, France), and D. Granier (Institut Gerhardt, Université Montpellier 2) for their help in the sample preparation and data collection.

The authors would like also to thank the ANR for financial support (Contract ANR-07-BLAN0258-PIEZOCRIST).

REFERENCES

(1) Cambon, O.; Goiffon, A.; Philippot, E. *J. Solid State Chem.* **1989**, *78*, 187−191.
(2) Philippot, E.; Goiffon, A.; Ibanez, A.; Pintard, M. *J. Solid State Chem.* **1994**, *110*, 356.
(3) Philippot, E.; Goiffon, A.; Ibanez, A. *J. Cryst. Growth* **1996**, *160*, 268−278.
(4) Yot, P.; Cambon, O.; Balitsky, D.; Goiffon, A.; Philippot, E.; Capelle, B.; Détaint, J. *J. Cryst. Growth* **2001**, *224*, 294−302.
(5) Cambon, O.; Yot, P.; Balitsky, D.; Philippot, E.; Capelle, B.; Detaint, J. *Ann. Chim.—Sci. Mat.* **2001**, *26*, 79−84.
(6) Balitsky, D. V.; Philippot, E.; Papet, Ph.; Balitsky, V. S.; Pey, F. *J. Cryst. Growth* **2005**, *275*, 887−894.
(7) Beaurain, M.; Armand, P.; Papet, P. *J. Cryst. Growth.* **2006**, *294*, 396−400.
(8) Armand, P.; Beaurain, M.; Rufflé, B.; Menaert, B.; Papet, P. *Inorg. Chem.* **2009**, *48*, 4988−4996.
(9) Cambon, O.; Yot, P.; Ruhl, S.; Haines, J.; Philippot, E. *Solid State Sci.* **2003**, *5*, 469.
(10) Cambon, O.; Haines, J.; Fraysse, G.; Detaint, J.; Capelle, B.; Van Der Lee, A. *J. Appl. Phys.* **2005**, *97*, 0741101−7.
(11) Grimm, H.; Dorner, B. *J. Phys. Chem. Solids* **1975**, *36*, 407−413.
(12) Cambon, O.; Bhalerao, G. M.; Bourgogne, D.; Haines, J.; Hermet, P.; Keen, D. A.; Tucker, M. G. *J. Am. Chem. Soc.* **2011**, *133*, 8048−8056.
(13) Haines, J.; Cambon, O.; Philippot, E.; Chapon, L.; Hull, S. *J. Solid State Chem.* **2002**, *166*, 434−441.
(14) Haines, J.; Cambon, O.; Hull, S. Z. *Kristallogr.* **2003**, *218*, 193−200.
(15) Haines, J.; Cambon, O.; Prudhomme, N.; Fraysse, G.; Keen, D. A.; Chapon, L. C.; Tucker, M. G. *Phys. Rev.* **2006**, *B 73*, 014103−10.
(16) Barz, R.-U.; Schneider, J.; Gille, P. *Z. Kristallogr.* **1999**, *214*, 845−849.
(17) Krempl, P. W.; Schleinzer, G.; Wallnofer, W. *Sens. Actuators* **1997**, *A61*, 361−363.
(18) Nakae, H.; Kihara, K.; Okuno, M.; Hirano, S. *Z. Kristallogr.* **1995**, *210*, 746−753.
(19) Smirnov, M.; Mazhenov, N.; Aliouane, N.; Saint-Grégoire, P. *J. Phys.: Condens. Matter* **2010**, *22*, 225403−225413.
(20) Roncal-Herrero, T.; Rodriguez-Blanco, J. D.; Benning, L. G.; Oelkers, E. H. *Cryst. Growth Des.* **2009**, *9*, 5197−5205.
(21) Zaghib, K.; Julien, C. M. *J. Power Sources* **2005**, *142*, 279−284.
(22) Liu, H. *J. Nanopart. Res.* **2010**, *12*, 2003−2006.
(23) Miclau, M.; Bucur, R.; Vlazan, P.; Miclau, N.; Trusca, R.; Grozescu, I. *J. Optoelectron. Adv. Mater.* **2007**, *9*, 2792−2794.
(24) Shafer, E. C.; Shafer, M. W.; Roy, R. *Z. Kristallogr.* **1956**, 107.
(25) Fursenko, B. A.; Kirkinsky, V. A.; Rjaposov, A. P. High-Pressure Science and Technology. *Proc. 7th AIRAPT Int. Conf.* Vodar, B., Marteau, P., Eds.; Pergamon: Oxford, U.K., 1980; p 562.
(26) Ranieri, V.; Bourgogne, D.; Darracq, S.; Cambon, M.; Haines, J.; Cambon, O.; Leparc, R.; Levelut, C.; Largeteau, A.; Demazeau, G. *Phys. Rev. B* **2009**, *79*, 224304−224313.
(27) Ranieri, V.; Haines, J.; Cambon, O.; Levelut, C.; Le Parc, R.; Cambon, M.; Hazemann, J.-L. *Inorg. Chem.* **2012**, *51*, 414−419.
(28) Haines, J.; Chateau, C.; Léger, J. M.; Marchand, R. *Ann. Chim.—Sci. Mat.* **2001**, *26*, 209−216.
(29) Veksler, I. V.; Thomas, R.; Wirth, R. *Am. Mineral.* **2003**, *88*, 1724−1730.
(30) Cachau-Herreillat, D.; Bennazha, J.; Goiffon, A.; Ibanez, A.; Philippot, E. *Eur. J. Solid State Inorg. Chem.* **1992**, *29*, 1295.
(31) Barz, R. U.; David, F.; Schneider, J.; Gille, P. *Z. Kristallogr.* **2001**, *216*, 501.
(32) O'Keeffe, M.; Hyde, B. G. *Acta Crystallogr.* **1978**, *B34*, 3519−3528.
(33) Haines, J.; Cambon, O.; Cachau-Herreillat, D.; Fraysse, G.; Mallassagne, F. E. *Solid State Sci.* **2004**, *6*, 995−999.
(34) Mohamed, F. Sh. *Adsorpt. Sci. Technol.* **2002**, *20*, 741.
(35) Bruyère, R.; Prat, A.; Goujon, C.; Hazemann, J.-L. *J. Phys.: Conf. Series* **2008**, *121*, 122003−4.
(36) Sham, T. K.; Hastings, J. B.; Perlman, M. L. *J. Am. Chem. Soc.* **1980**, *102*, 5904−5906.
(37) Apted, M. J.; Waychunas, G. A.; Brown, G. E. *Geochim. Cosmochim. Acta* **1985**, *49*, 2081−2089.
(38) Lindqvist-Reis, P.; Muñoz-Páez, A.; Díaz-Moreno, S.; Pattanaik, S.; Persson, I.; Sandström, M. *Inorg. Chem.* **1998**, *37* (26), 6675−6683.
(39) Proux, O.; Biquard, X.; Lacera, E.; Menthonnex, J. J.; Prat, A.; Ulrich, O.; Soldo, Y.; Trevisson, P.; Kapoujyan, G.; Perroux, G.; Taunier, P.; Grand, D.; Jeantet, P.; Deleglise, M.; Roux, J. P.; Hazemann, J.-L. *Phys. Scr.* **2005**, *T115*, 970−973.
(40) Proux, O.; Nassif, V.; Prat, A.; Ulrich, O.; Lahera, E.; Biquard, X.; Menthonnex, J.-J.; Hazemann, J.-L. *J. Synchrotron Radiat.* **2006**, *13*, 59−68.
(41) Testemale, D.; Argoud, R.; Geaymond, O.; Hazemann, J.-L. *Rev. Sci. Instrum.* **2005**, *76*, 043905−043909.

(42) http://webbook.nist.gov/chemistry/.
(43) Rehr, J. J.; Albers, R. C. *Rev. Mod. Phys.* **2000**, *72*, 621−654.
(44) Elam, W. T.; Ravel, B.; Sieber, J. R. *Radiat. Phys. Chem.* **2002**, *63*, 121−128.
(45) Ravel, B.; Newville, J. M. *J. Synchrotron Radiat.* **2005**, *12*, 537−541.
(46) Sheldrick, G. M.; Schneider, T. R. *Methods Enzymol.* **1997**, *277*, 319−343.
(47) Wilke, M.; Farges, F.; Petit, P.-E.; Brown, G. E.; Martin, F. *Am. Mineral.* **2001**, *86*, 714−730.
(48) Cochain, B.; Neuville, D. R.; Roux, J.; de Ligny, D.; Testemale, D.; Pinet, O.; Richet, P. *Mater. Res. Soc. Symp. Proc.* **2009**, 1124.
(49) Lucas, H.; Petitet, J.-P. *J. Phys. Chem. A* **1999**, *103*, 8952−8958.
(50) Pokrovski, G. S.; Schott, J.; Hazemann, J.-L.; Farges, F.; Pokrovsky, O. S. *Geochim. Cosmochim. Acta* **2002**, *66*, 4203−4322.
(51) Song, Y.; Zavalij, P. Y.; Suzuki, M.; Whittingham, S. M. *Inorg. Chem.* **2002**, *41*, 5778−5786.
(52) O'Keefe, M.; Navrotsky, A. *Structure and Bonding in Crystals*; Academic Press: New York, 1981.
(53) Haouas, M.; Taulelle, F.; Prudhomme, N.; Cambon, O. *J. Cryst. Growth* **2006**, *296* (2), 197−206.
(54) Philippot, E.; Palmier, D.; Pintard, M.; Goiffon, A. *J. Solid State Chem.* **1996**, *123*, 1−13.
(55) Shannon, R. D. *Acta Crystallogr.* **1976**, *A32*, 751−767.